Applied Materials Today 23 (2021) 101017

Contents lists available at ScienceDirect

Applied Materials Today

journal homepage: www.elsevier.com/locate/apmt

2D $MoTe_2$ nanosheets by atomic layer deposition: Excellent photo-electrocatalytic properties

Raul Zazpe[a,b,*], Hanna Sopha[a,b], Jaroslav Charvot[c], Richard Krumpolec[d], Jhonatan Rodriguez-Pereira[a,b], Jan Michalička[b], Jan Mistrík[a], Dominik Bača[d], Martin Motola[a], Filip Bureš[c], Jan M. Macak[a,b]

[a] Center of Materials and Nanotechnologies, Faculty of Chemical Technology, University of Pardubice, Nam. Cs. Legii 565, 53002 Pardubice, Czech Republic
[b] Central European Institute of Technology, Brno University of Technology, Purkynova 123, 61200 Brno, Czech Republic
[c] Institute of Organic Chemistry and Technology, Faculty of Chemical Technology, University of Pardubice, Studentská 573, 53210, Pardubice, Czech Republic
[d] Department of Physical Electronics, CEPLANT — R&D Center for Plasma and Nanotechnology Surface Modifications, Faculty of Science, Masaryk University, Kotlářská 267/2, 61137 Brno, Czech Republic

ARTICLE INFO

Article history:
Received 11 December 2020
Revised 12 March 2021
Accepted 18 March 2021

Keywords:
$MoTe_2$
nanosheets
Atomic Layer Deposition
TiO_2 nanotube layers
catalysis

ABSTRACT

Herein, the synthesis of $MoTe_2$ nanosheets by means of Atomic Layer Deposition (ALD) is demonstrated for the first time. ALD enables tight control over the thickness and the composition of the deposited material, which are highly appealing features for the nanostructure fabrication. The growth of ALD $MoTe_2$ was studied on substrates of different nature, including TiO_2 nanotube (TNT) layers used as active supporting material for fabricating hierarchical nanotubular $MoTe_2$/TNT heterostructure. The combination of newly synthesized Te precursor with commercial Mo precursor rendered the growth of 2D flaky $MoTe_2$ nanosheets mostly out-of-plane oriented. The as-deposited $MoTe_2$ was extensively characterized by different techniques which confirmed its chemical composition and revealed 2D flaky nano-crystalline structures. In parallel, $MoTe_2$/TNT layers were employed to explore and exploit both photo- and electrocatalytic properties. The synergy stemming from the out-of-plane $MoTe_2$ nanosheet orientation, with an optimized amount of catalytic active edges, and the fast electron transfer through 1D TiO_2 nanotubes triggered the catalytic properties for both, organic pollutant degradation and hydrogen evolution reaction (HER) applications. Remarkably, the application of a cathodic potential originated a gradual HER electrochemical activation over time driving to a higher current density and an overpotential drop.

1. Introduction

Following the discovery of graphene, significant efforts focused on the search and development of alternative two-dimensional (2D) materials [1,2]. The unique structural, optical and electronic properties that 2D materials offer in comparison with their bulk counterparts, open new opportunities in a large number of applications ranging from optoelectronics and catalysis to sensing and nanoelectronics [3–8]. Transition metal dichalcogenides (TMDs) are one of the most encouraging members of the 2D family and materials developed. When compared to bulk materials, they possess outstanding catalytic properties with greater activity, selectivity and stability, together with extremely enhanced surface-to-volume ratio and the capability of tuning their catalytically active edge sites [9,10]. Importantly, they represent an affordable earth-abundant alternative to replace the expensive and low abundance Pt group metals [11,12]. 2D TMDs have the composition MX_2 (M = Mo or W; X = S, Se, or Te) and layered structure where a single layer is comprised of a transition metal atoms sheet sandwiched between two sheets of chalcogen atoms. The intralayer M-X bonds are covalent whereas the layers are held together by weak van der Waals forces [2]. In the last years, 2D TMDs such as WS_2, MoS_2 and $MoSe_2$ have been well-studied materials that have attracted growing interest due to its fascinating properties towards catalytic applications [13–17]. In contrast, the telluride equivalent

* Corresponding author at: Center of Materials and Nanotechnologies, Faculty of Chemical Technology, University of Pardubice, Nam. Cs. Legii 565, 530 02 Pardubice, Czech Republic.
E-mail address: raul.zazpe@upce.cz (R. Zazpe).

https://doi.org/10.1016/j.apmt.2021.101017

$MoTe_2$ has been barely studied and has never been synthesized by Atomic Layer Deposition (ALD) until this report. $MoTe_2$ possesses two stable structures at room temperature, namely semiconducting hexagonal (2H) and metallic monoclinic (1T′) phases, the latter presenting a distorted octahedral coordination around each Mo atom [18]. The small formation energy (~0.03 eV) required for the phase transformation between the 2H and the 1T' structures gives outstanding phase transition abilities to $MoTe_2$ [19]. As to optical properties, bulk $MoTe_2$ owns a semiconducting nature with an indirect band gap value of about 1 eV (comparable to Si), while in the monolayer case the direct band gap value is 1.1 eV, which is smaller than that of MoS_2 (1.8 eV) and $MoSe_2$ (1.88 eV) [20,21]. The electronic conductivity of Te is superior as compared to S and Se, and a field effect mobility as high as 40 $cm^2\ V^{-1}\ s^{-1}$ has been reported at room temperature [22]. Those properties have promoted the application of $MoTe_2$ in (opto-)electronic devices, (photo)gas sensors and photoelectrochemical cells [23–32]. In parallel, great prospects are deposited in energy storage applications such as, alkaline-ionic (Li and Na) batteries and supercapacitors, based on layered $MoTe_2$ with an interlayer spacing of ~0.7 nm, larger than that one of graphene (0.335 nm), MoS_2 (0.615 nm) and $MoSe_2$ (0.646 nm) [33–38]. The wider interlayer spacing reduces the energy barrier and the ion diffusion resistance in the electrodes. Additionally, $MoTe_2$ holds encouraging promises in catalytic applications, in particular towards hydrogen evolution reaction (HER), basically due its excellent carrier transport properties and low Gibbs free energy of hydrogen adsorption [39–48]. However, the performance of bulk $MoTe_2$ is limited by the low density of electrocatalytic active sites. A strategy to circumvent those limitations is the synthesis of 2D layered $MoTe_2$ that brings about an important increase of the surface area and the number of catalytic actives sites [49]. Different methods have been reported for the synthesis of nanostructured $MoTe_2$ including top-down methods such as mechanical and liquid exfoliation [20,25,46,50], and bottom-up methods, such as reaction of the individual elements under thermal treatment [36,42,43,51], microwave-synthesis [44], electrodeposition [34,47], flux method [40], tellurization of Mo or Mo oxide films [52,53], sputtering [18], molecular beam epitaxy (MBE) technique [54] and chemical vapor deposition (CVD) [48,53]. The resulting $MoTe_2$ has been reported to exhibit varying Mo:Te values, mainly estimated from XPS analysis, exhibiting a whole range of stoichiometries (from a slight excess or deficiency of Te [34,47] to stoichiometric values [48,53]). The impact of Te vacancies on electrocatalytic performance has been explored in a recent work, that described the stoichiometric $MoTe_2$ (Mo:Te ratio value 1:2) outperformed sub-stoichiometric $MoTe_2$, suggesting that the hydrogen adsorption occurs preferentially on the tellurium sites [43]. Although aforementioned methods reported successful $MoTe_2$ synthesis, they show different limitations. While the main disadvantages of both liquid and mechanical exfoliation methods lie on the difficult scale up and the small size of the flakes, wet chemical methods are generally time consuming, use surfactants and it is hard to obtain uniform single-layer nanosheet. Regarding sputtering and electrodeposition methods, poor large-area uniform thickness and conformality are the main drawbacks, respectively. Besides, alternative approaches based on energy irradiation or etching oriented to increase the number of $MoTe_2$ active edges sites are strongly limited by the great tendency to oxidation of $MoTe_2$. In contrast, gas phase methods such as chemical vapor deposition attracted interest for pseudo large-area growth, but the main disadvantages are the lack of homogeneity of the material deposited and a limited thickness control, which can be enhanced by MBE technique. Thus, ALD is the only vapor phase deposition technique meeting a following set of requirements: precise thickness control, and uniform and conformal deposition including high aspect-ratio and 3D nanostructures. Consequently, ALD is the deposition method of choice by far to attain uniform and conformal deposition on high surface-area and complex shape substrates.

ALD is a well-established deposition technique that in contrast to CVD, is based on alternating gas-surface chemical reactions of self-limiting nature. The gas chemical precursors are introduced separately to react with the substrate, followed by a purging step with an inert carrier gas (N_2 or Ar) preventing potential gas phase reactions in between the precursors. The limited number of active surface sites leads to a self-limiting chemical reaction and limits the material growth of an ALD cycle up to a monolayer. The ALD cycle is repeated until the desired material thickness is attained. The main benefits of ALD over other deposition techniques (e.g. CVD or physical vapor deposition (PVD)) stem from the self-limiting feature of ALD, which allows exceptional control over the thickness and enables depositing materials in a conformal and uniform fashion on high aspect ratio and 3D structured materials [55–57]. In the last years, significant efforts have been devoted to the ALD synthesis of 2D materials (including oxides, sulphides, selenides and tellurides), being TMDs one of the most promising 2D materials family for a wide number of applications. Some recent reviews provide more detailed information [58–60].

Herein, the synthesis of $MoTe_2$ by ALD is demonstrated for the first time using novel Te precursor and commercial Mo precursor. The as-deposited $MoTe_2$ grew as 2D flaky nanosheets (increasing strongly the number of edge sites) mostly out-of-plane oriented (maximizing the exposed active edges). Rationally designed hierarchical structures ALD $MoTe_2$/1D TiO_2 nanotube layers (TNT layers) were fabricated in a simple and fast fashion in order to assess and exploit the photo- and electrochemical properties of ALD synthesized $MoTe_2$ nanosheets. The choice of TNT layers (5 μm-thick) as supporting platform was based on the synergistic effect basically due to the unique tubular architecture, enhanced charge transfer, the semiconducting nature of TiO_2, chemical stability and high surface-area ratio. Hence, the combination of ALD $MoTe_2$ nanosheets deposited on 1D TNT layers yielded superior photo- and electrocatalytic properties, verifying the synergistic properties for both, organic dye degradation and HER applications. Notably, a gradual electrochemical activation was observed under applying both, a constant cathodic potential and a potential sweep via cyclic voltammetry.

2. Experimental methods

2.1. TiO_2 nanotube layers fabrication

The self-organized TNT layers were fabricated via electrochemical anodization of Ti foils as described in our previous works [61]. The as-prepared amorphous 5 μm-thick TNT layers turned into anatase phase upon post-annealing process in a muffle oven at 400 °C for 1 h [62].

2.2. Synthesis of Te precursor

Cyclic silyltelluride was prepared via a modified procedure similar to that reported by Herzog and Rheinwald (Scheme 1) [63]. The synthesis was carried out under strictly argon atmosphere and freshly distilled solvents were always used. Target Te-precursor **1** is a moisture- and light-sensitive compound. However, no decomposition was observed if stored under an inert atmosphere at –5 °C for one month. This is in high contrast to formerly reported extremely high air- and light-sensitive $(Me_3Si)_2Te$ or $(Et_3Si)_2Te$ that we have also encountered [64]. The latter two silyltellurides are currently the most used Te precursors for ALD [65–67]. Differential scanning calorimetry (DSC) measurement of **1** showed good volatility without decomposition (see the Supporting Information, Figs. S1–S6, for more details).

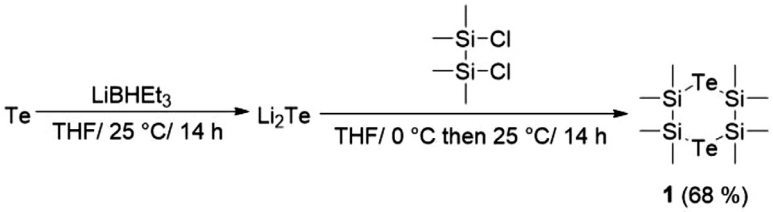

Scheme 1. Reaction pathway towards cyclic silyltelluride **1**.

2.3. Synthesis of $MoTe_2$ by atomic layer deposition

The deposition of $MoTe_2$ was carried out in a custom-made thermal ALD system at chamber pressure 2 mbar applying a deposition temperature of 270 °C. The growth of ALD $MoTe_2$ was studied on different substrates: microscope blank glass slides, annealed titanium foil, silicon wafer and TNT layers. The Mo precursor was $MoCl_5$ (Strem, anhydrous 99.6%), and novel cyclic silyltelluride **1** was used as the Te precursor (see the Supporting Information for its synthesis). They were heated up to get sufficiently high vapor pressure at 120 and 175 °C, respectively. Immediately before starting the ALD process, 5 pulses (500 ms) of ultrapure water (18 MΩ cm^{-1}) were applied to increase the number of hydroxyl active sites on the substrates surface. One ALD cycle was defined by the subsequent sequence: Te precursor (1 s) – N_2 purge (5 s) – Mo precursor (800 ms) – N_2 purge (5 s). The number of cycles applied were 20, 60, 180, 250, 360, 500, 540, 1000 and 1500. N_2 (99.999%) was used as carrier gas at a flow rate of 40 standard cubic centimetre per minute (sccm). Additionally, ALD processes applying different Te dose (for a Mo dose constant of 800 ms) were conducted, namely 250, 1000 and 1500 ms. Corresponding SEM top view images from annealed Ti foils and Si wafer, together with the SEM cross-section of the Si wafer, are shown in the Fig. S7. The proposed gas-to-solid phase reaction mechanism of cyclic silyltelluride **1** with $MoCl_5$ involves favourable exchange of Lewis acid-base pairs as predicted previously by Pore et al. [65]. The growth of $MoTe_2$ is accompanied by a formation of volatile 1,2-dichlorotetramethyldisilane as by-product (see Scheme S1 in the Supporting Information).

2.4. Characterization techniques

The evaluation of the structure and morphology of the $MoTe_2$ TNT layers was conducted by field emission scanning electron microscope (FE-SEM) JEOL JSM 7500F and a high-resolution transmission electron microscope (HRTEM) Thermo Fisher Scientific Titan Themis 60–300, operated at 300 kV and equipped with a C_s image aberration corrector, a high angle annular dark field detector for scanning transmission electron microscopy (STEM-HAADF) imaging, and Super-X energy dispersive X-ray (EDX) spectrometer with four 30 mm^2 windowless detectors for STEM-EDX analysis.

The surface chemical composition of $MoTe_2$ was monitored by X-ray photoelectron spectroscopy (XPS) (ESCA2SR, Scienta-Omicron) using a monochromatic Al Kα (1486.7 eV) X-ray source. The binding energy (BE) scale of the spectra was corrected taking the Mo-Te component peak at 227.7 eV in Mo 3d as a Ref. [68]. The data analysis was performed with CasaXPS program (Casa software Ltd).

X-ray diffraction (XRD) analysis was carried out using Panalytical Empyrean with Cu tube and Pixcel3D detector. Grazing incidence XRD was performed to obtain diffraction peaks of the as-deposited $MoTe_2$. The incident angle was 1°. The patterns were recorded in range of 5 – 65°, step size was 0.026°.

Spectroscopic ellipsometry was carried out on VASE ellipsometer (Woollam Ltd.) for various incidence angles (50°, 60°, 70°, 80°) and in spectral range covering NIR, VIS and UV. Besides ellipsometry parameters also nearly normal incidence reflectance spectra were recorded with the same instrument. All obtained optical spectra were numerically treated simultaneously by VASE software.

The photoresponse measurements of $MoTe_2$ TNT layers were carried out in an aqueous 0.1 M Na_2SO_4 at 0.4 V vs. Ag/AgCl in the spectral range from 300 to 800 nm. A photoelectric spectrophotometer (Instytut Fotonowy) with a 150 W Xe lamp and a monochromator with a bandwidth of 10 nm connected with a modular electrochemical system AUTOLAB (PGSTAT 204; MetrohmAutolab B. V.; Nova 1.10 software) was used for the photoresponse measurements. Photocurrent stability tests were carried out by measuring the photocurrent produced under chopped light irradiation (light/dark cycles of 10 s).

The photodegradation of methylene blue solution (MB, initial concentration 1×10^{-5} M) was used to determine photocatalytic degradation activities of all samples. Prior to all measurements, dye adsorption/desorption equilibrium was attained by immersing the samples in 3.5 mL of the MB solution for 60 min with constant stirring. Afterwards, the samples were irradiated by a LED-based UV lamp (10 W, λ=365 nm ± 5 nm) or VIS lamp (10 W, λ=410–425 nm). An UV–VIS spectrometer (S-200, Boeco) at a wavelength of 670 nm was employed to determine the absorbance of the MB solution periodically (10 or 30 min steps) to monitor the degradation rate.

The electrocatalytic activity of the $MoTe_2$/TNT layers towards HER was evaluated by cyclic voltammetry (CV) in 0.5 M H_2SO_4 in the potential range from +0.1 V to −1 V vs Ag/AgCl using a standard three electrode setup. The scan rate was 2 mV/s. The first negative scan for all $MoTe_2$/TNT layers is shown in the polarization curves. The potentials were quoted against the reversible hydrogen electrode (RHE) using the Eq. (1), and the current densities were normalized to the macroscopic surface area of the samples exposed to the solution.

$$E_{RHE} = E + (0.059\ V)\ pH + E^0{}_{ref\ vs\ SHE} \quad (1)$$

with $E^0{}_{ref\ vs\ SHE}$ = 0.237 V, being the standard potential of the Ag/AgCl reference electrode vs the standard hydrogen electrode (SHE).

Chronoamperometry was carried out for the TNT layers coated with 250 and 1500 $MoTe_2$ ALD cycles in 0.5 M H_2SO_4 at −550 mV for 48 h. The potentials were converted to the reversible hydrogen electrode (RHE) scale by using the Eq. (1).

3. Results and discussion

3.1. Characterization

The morphology characterization of the as-deposited $MoTe_2$ was carried out by means of SEM. The growth of $MoTe_2$ by ALD was explored on substrates of different nature such as, glass, annealed Ti foil (with TiO_2 surface in the anatase phase) and silicon wafer (with SiO_2 surface). As-deposited $MoTe_2$ exhibited 2D flaky nanosheets structure randomly oriented regardless the substrate as

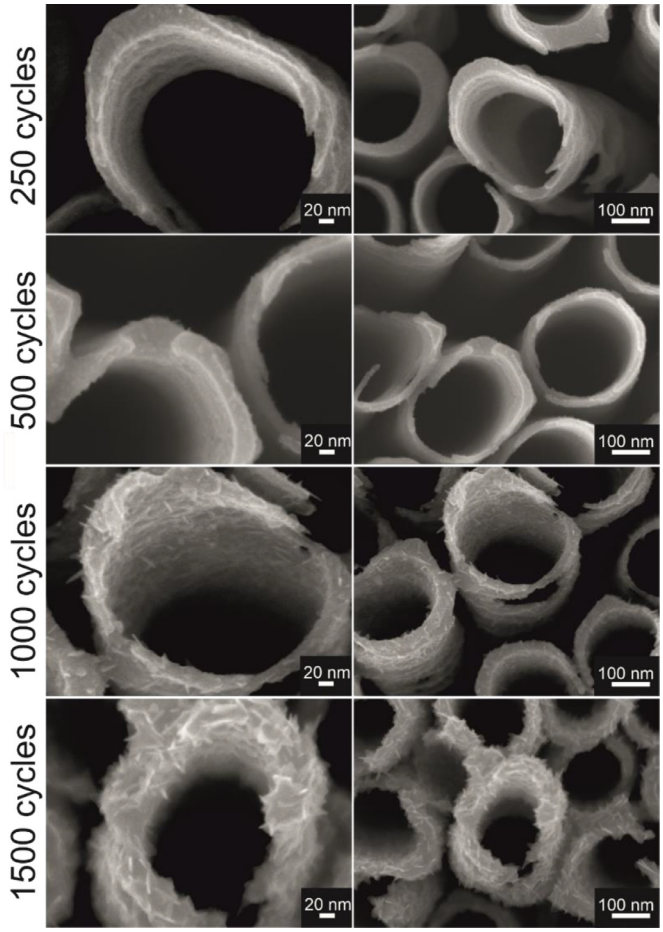

Fig. 1. SEM top-view images at two different magnifications of the 5 μm-thick TNT layers decorated with a different number of $MoTe_2$ ALD cycles: 250, 500, 1000 and 1500.

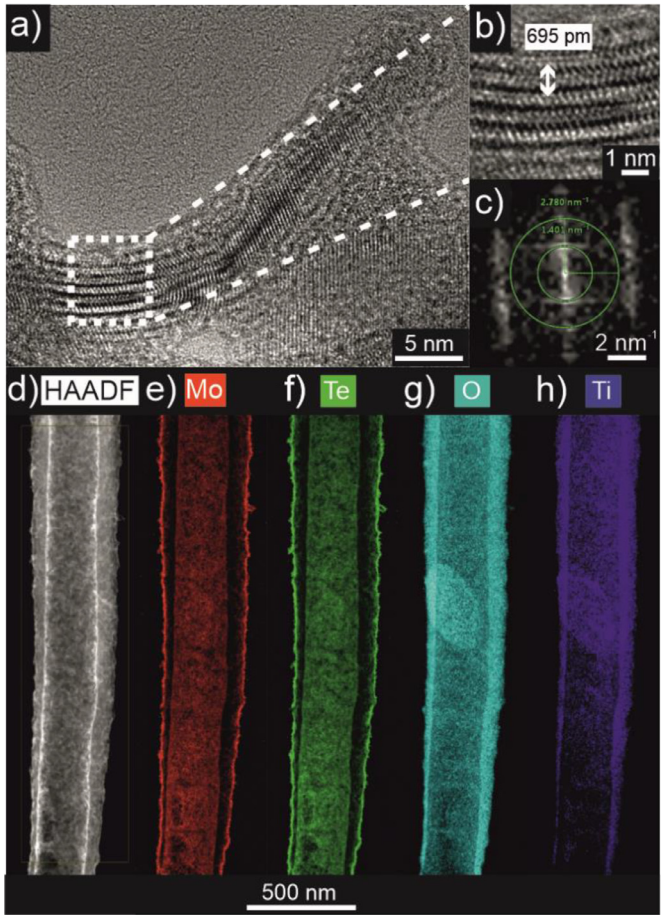

Fig. 2. (a) HR-TEM image showing the multilayered $MoTe_2$ nanostructure deposited upon 1500 ALD cycles; (b) Locally amplified HR-TEM of the multilayered $MoTe_2$ nanostructure, where an interlayer spacing of around 0.69 nm was estimated; (c) corresponding Fast Fourier Transform pattern, where the measured radii 1.401 nm^{-1} and 2.780 nm^{-1} were about 0.71 nm in the real space value, confirming the as-deposited $MoTe_2$ interlayer spacing (≈ 0.7 nm); d) STEM HAAD image of a fragment of 5 μm-thick TNT decorated with $MoTe_2$ nanosheets upon 1500 ALD cycles; (e–h) The corresponding STEM EDX elemental maps which exhibit the distribution of (e) Mo(L), (f) Te(L), (g) O(K) and (h) Ti(K).

shown in the Fig. S8. Likewise, TiO_2 nanotube layers (TNT layers) decorated with a different number of $MoTe_2$ ALD cycles were characterized by SEM, as displayed in Fig. 1.

Therein, one can observe how $MoTe_2$ nanosheets decorated the inner and outer parts of the TNTs surface including the deepest (bottom) inner part (Fig. S9), and their growth along with an increasing number of ALD cycles. Unambiguously, the $MoTe_2$ revealed a 2D flaky structure when a high ALD cycle number was employed. As-deposited $MoTe_2$ deposited on TNT layers upon 1500 ALD cycles were characterized by transmission electron microscope (TEM), revealing multilayered $MoTe_2$ nanostructure as shown in Fig. 2a-b. Characteristic interlayer distance, estimated from the HR-TEM image, was ca. 0.69 nm (Fig. 2b). This distance was further confirmed by the corresponding Fast Fourier transform (FFT) measurements (Fig. 2c), and revealed a great match with $MoTe_2$ interlayer spacing (0.7 nm). The energy-dispersive X-ray spectroscopy (EDX) elemental map allowed to confirm the uniform and homogeneous presence of Mo (Fig. 2e) and Te (Fig. 2f) species all along the TNT walls upon 1500 ALD cycles. Additionally, STEM EDX analysis was conducted in the selected area, marked in Fig. S10a, in order to determine the chemical composition of the as-deposited $MoTe_2$ nanosheets. Fig. S10b and c show a high-magnification bright field TEM image and STEM-elemental map of the area enclosed, respectively. The latter exhibits a color-mix overlay of Ti-Mo-Te maps allowing to discern the interface between the TNT and the as-deposited $MoTe_2$, which is characterized by EDX in two different areas, denoted as area 1 and 2. The Mo and Te quantification was based on the L lines Mo(L) and Te(L) from the corresponding EDX spectra shown in Fig. S11. The resulting Te:Mo ratio values of ≈ 1.7 (area #1) and ≈ 1.5 (area #2) calculated from the corresponding quantification (shown in Table S1), suggested sub-stoichiometric $MoTe_2$ with Te deficiency (dichalcogenide vacancies).

Grazing Incident X-Ray Diffractometry (GI-XRD) revealed polycrystalline nature of the as-deposited $MoTe_2$ upon 1500 ALD cycles on TNTs. The diffraction peaks observed in the GI-XRD pattern (Fig. S12) at 2θ ~ 12.2°, ~29.2°, ~32.3° and ~50.8° matched well with the (002), (100), (102) and (110) planes. GI-XRD patterns corresponding to TNT layers decorated with lower a number of $MoTe_2$ ALD cycles only exhibited TiO_2 anatase diffraction peaks. This was ascribed to the small crystalline domains within the $MoTe_2$.

The surface chemical composition of the as-deposited $MoTe_2$ nanosheets was analysed by X-Ray Photoelectron Spectroscopy (XPS). Fig. S13 shows the XPS survey spectra for 180, 360 and 1500 $MoTe_2$

ALD cycles, where traces of Si indicate the minor presence of reaction by-products (Te-precursor **1** contains Si atoms). The left column of Fig. 3 shows the deconvolution of the XPS high resolution spectra of Mo 3d obtained from the TNT layers decorated with 180, 360 and 1500 $MoTe_2$ ALD cycles. Valuable insight into the chemical composition of the ALD $MoTe_2$/TNT layers surface was provided by detailed deconvolution, in particular for the low-cycle

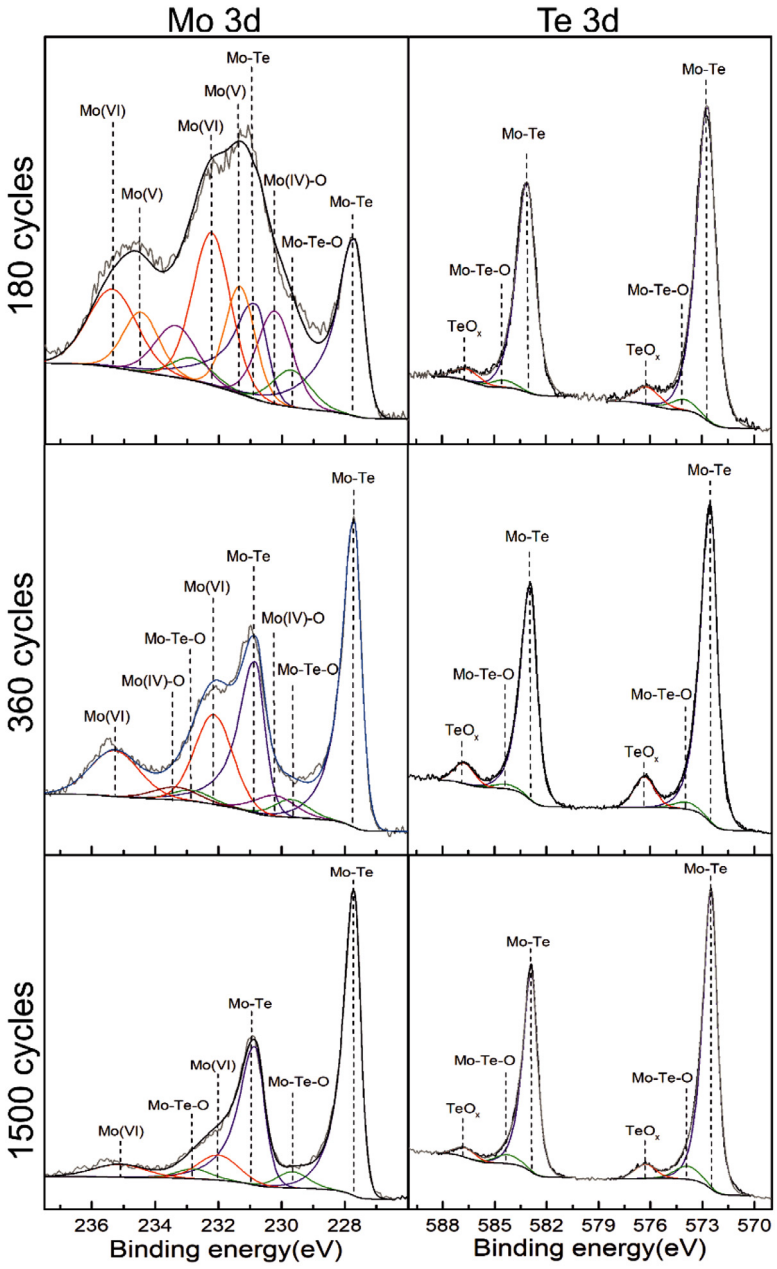

Fig. 3. XPS high-resolution spectra of deconvoluted Mo 3d and Te 3d peaks corresponding to 180, 360 and 1500 $MoTe_2$ ALD cycles.

ALD processes (180 and 360 ALD cycles). Mo(IV)-Te exhibited two peaks at 227.7 and 230.8 eV corresponding to spin-orbit splitting Mo $3d_{5/2}$ and Mo $3d_{3/2}$ confirming the growth of $MoTe_2$. The asymmetric shape in the Mo 3d signal, observed in the components corresponding to the Mo-Te bonds, has been previously ascribed to 1T' $MoTe_2$ phase [18,69–71]. Significantly, the chemical reaction of both, the Te precursor with the hydroxyl groups and the following reaction of the resulting chemisorbed counterpart with the Mo precursor was confirmed by the peak corresponding to the presence of Mo-Te-O bonds ~229.7 eV ($Mo3d_{5/2}$). Additional peaks revealed the presence of different chemical environments. Thus, the binding energies (BE) corresponding of these peaks matched well with the presence of Mo(VI) at ~232.2 eV ($Mo3d_{5/2}$), Mo(V) at ~231.3 eV ($Mo3d_{5/2}$) and Mo(IV)-O bonds at ~230.2 eV ($Mo3d_{5/2}$). The origin of those species is ascribed to a substrate interface effect stemming from the low-cycle ALD stage, when remaining available hydroxyl groups from the TNT layers surface reacted with $MoCl_5$ as it was introduced into the ALD chamber, in line with observations in a recent work [72]. Along with an increasing number of ALD cycles a strong fading of those peaks takes place, indicating that the formation of embedded MoO_x species was restricted to a substrate interface effect (the only source of hydroxyl groups). The right column of Fig. 3 contains the corresponding deconvoluted XPS high resolution spectra of Te 3d. The deconvolution allowed to identify the presence of (i) two main Te-Mo peaks located at ~572.5 eV and ~582.9 eV attributed to Te $3d_{5/2}$ and Te $3d_{3/2}$ confirming the deposition of $MoTe_2$, (ii) Mo-Te-O bonds at ~573.9 eV and ~584.3 eV corroborating the chemical reaction between both Mo and Te precursors; (iii) two small peaks at ~576.3 eV and ~586.7 eV corresponding to Te-O bond. The lack of any oxygen source during the ALD process (use of oxygen-free precursors) and the strong tendency towards oxidation would suggest that the origin of the Te-O bond is due to the exposition to air [73]. Fig. S14 shows the XPS high-resolution spectra of deconvoluted Mo 3d and

Te 3d peaks corresponding to titanium foil and silicon wafer upon deposition of 1500 $MoTe_2$ ALD cycles verifying the ALD deposition of $MoTe_2$.

3.2. Photoelectrochemical properties

The photoelectrochemical characterization of blank and ALD $MoTe_2$/TNT layers was conducted in the wavelength range from 300 to 800 nm. The obtained incident photon-to-electron conversion efficiencies (IPCE) are shown in Fig. S15a. Significant IPCE values of up to 65% and 70% were recorded upon 20 and 60 $MoTe_2$ ALD cycles respectively, in comparison with the blank counterpart (up to 34%) in the UV region. As to the visible spectral region, the high band gap energy of anatase TiO_2 E_g~3.2 eV (≈ 387 nm) hindered the photoresponse of the blank TiO_2 NTs, while extended photoresponse was observed for TNT layers decorated with 180 $MoTe_2$ ALD cycles, being photoactive in the visible light range due to a narrower band gap. The enhancement of the photoelectrochemical properties in the UV region after the deposition of few $MoTe_2$ ALD cycles is ascribed to the effective passivation of the surface defects (oxygen vacancies and traps) within the TNT walls upon low-cycle $MoTe_2$ ALD stage [74–76]. Such surface defect passivation, together with the band offset at the $MoTe_2/TiO_2$ interface and the associated built-in electric field drive to efficient charge carrier separation (longer lifetimes of the photo-generated charge carriers) resulting in a more effective separation, transfer and collection of the charge carriers, as demonstrated by a superior photoresponse. However, the deposition of 360 $MoTe_2$ ALD cycles was found detrimental to the photoelectrochemical properties, and led to lower IPCE values. It is mainly ascribed to a growing number of stacking $MoTe_2$ layers, which basically depresses both the charge carrier separation efficiency, and the inherent low electron conductivity in perpendicular direction to the basal $MoTe_2$ planes. The separation efficiency of the photo-generated charge carriers was further assessed via photocurrent transients recorded over a range of wavelengths both in UV (350–370 nm) and visible (400–420 nm) region (see Fig. S15b). The ALD $MoTe_2$ TNT layers displayed higher photocurrent response than that of the blank counterpart. The improved charge carrier separation efficiency produced by the deposition of $MoTe_2$ was confirmed by a sharp photocurrent density increase/drop under ON/OFF irradiation cycles, both in the UV and visible light regions.

3.3. Optical properties

Ellipsometric and reflectance spectra were modelled against a model sample consisting of c-Si substrate covered by 2D $MoTe_2$ nanostructured film. The thin native oxide of c-Si substrate fitted well with the thickness determined by preliminary measurements on blank Si substrate. The 2D nanostructured $MoTe_2$ film was modelled as an homogenous single layer with optical constants approximated by two-phase ($MoTe_2$ and voids) Bruggeman effective medium theory [77]. Dielectric function of $MoTe_2$ was parameterized by the sum of two Gauss and one Drude oscillators. Value of filling factor of 50% was roughly estimated from the film surface topology. Simultaneous fitting of ellipsometry and reflectance spectra provided optical constants of 2D flaky $MoTe_2$ nanosheets, which are presented in Fig. S16 in the form of photon energy dependence of its refractive index and the extinction coefficient. Obtained spectra are close (in both spectral trends and absolute values) to recently reported complex refractive index of $MoTe_2$ synthetized in 1T' phase [78]. Moreover, they significantly differ from exciton populated optical constants of $MoTe_2$ in 2H phase. Therefore, we suppose that the 2D $MoTe_2$ flaky nanosheets investigated in this study present mainly semimetal character that corresponds to 1T' phase.

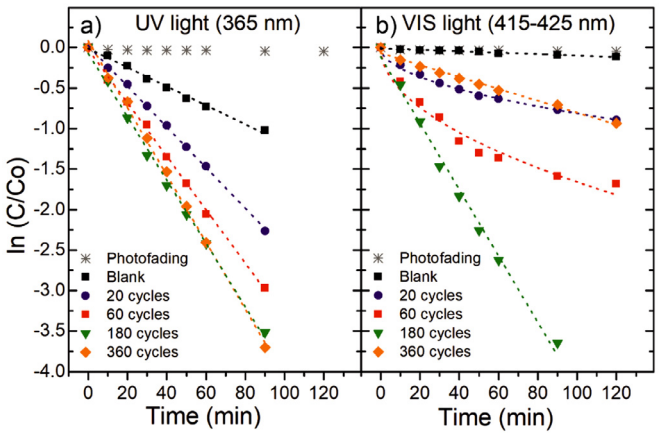

Fig. 4. Photocatalytic decomposition rates of MB for blank TNT layers and TNT layers decorated with 20, 60, 180 and 360 $MoTe_2$ ALD cycles under (a) UV light (365 nm) and (b) visible light (415–425 nm). Dashed lines are provided as a guide to the eye.

Table 1
Photocatalytic (pseudo-first order) kinetic rate constants (k) of MB degradation upon UV illumination (365 nm, LED array) for blank TNT layers and their counterparts decorated with a different number of $MoTe_2$ ALD cycles. The kinetic rate constant values were obtained by linear fitting of the curves exhibited in Fig. 4a.

Sample	k (min^{-1})
Blank	0.0117
20 ALD cycles	0.0251
60 ALD cycles	0.0330
180 ALD cycles	0.0391
360 ALD cycles	0.0414

3.4. Photocatalytic properties

The photocatalytic activity of the different ALD $MoTe_2$/TNT layers was explored by the photodegradation of an organic model dye (methylene blue, MB) under UV (365 nm) and visible light irradiation (410–425 nm). Fig. 4a displays the photocatalytic activity under UV light (365 nm) of both blank TNT layers and their ALD $MoTe_2$ decorated counterparts, exhibiting pseudo-first order degradation kinetic. A higher number of $MoTe_2$ ALD cycles drove to enhanced degradation kinetics, as reflected by the corresponding photocatalytic kinetic rate constants (shown in Table 1), obtained from the linear fitting of the curves (dashed lines):

$$ln\left(\frac{C}{Co}\right) = -kt \quad (2)$$

where C_o and C are MB concentrations at the beginning and at time t, respectively, and k is the pseudo-first order kinetic rate constant.

After 90 min, the original MB concentration was reduced down to approx. 36.0, 10.4, 5.15, 2.96 and 2.47% of its initial value for the blank TNT layers, and TNT layers decorated with 20, 60,180 and 360 $MoTe_2$ ALD cycles, respectively. MB degradation rates enhanced up to five times, as compared to the blank counterpart. The enhancement of the photocatalytic properties was based on a double effect provided by the deposition of $MoTe_2$ nanosheets, namely, (i) a higher incident light absorption and (ii) a greater amount of available redox active species, generated at the electrolyte-$MoTe_2$/TNT layers.

Table 2
Coefficient A (for TNT layers with 20 and 60 $MoTe_2$ ALD cycles) and constant (k) values (for TNT layers with 180 and 360 $MoTe_2$ ALD cycles) of MB degradation upon the visible light illumination (415–425 nm, LED array). The coefficient A and kinetics rate constant values were obtained by fitting of the curves shown in Fig. 4b.

Sample	k (min^{-1})	A^2 (min^{-1})
20 ALD cycles		0.0066
60 ALD cycles		0.0272
180 ALD cycles	0.0409	
360 ALD cycles	0.0073	

Table 3
Overpotential at the cathodic current density of 10 mA cm^{-2} and Tafel slope obtained for the TNT layers decorated with a different number of $MoTe_2$ ALD cycles in 0.5 M H_2SO_4 solution.

Sample	Overpotential for −10 mA cm^{-2} (mV)	Tafel slope (mV/dec)
60 ALD cycles	451	142
250 ALD cycles	373	108
500 ALD cycles	383	103
1000 ALD cycles	439	107
1500 ALD cycles	478	101

The MB photodegradation was performed also under visible light illumination (where TiO_2 is catalytically inactive) in order to evaluate the photocatalytic activity strictly ascribed to the $MoTe_2$ nanosheets photoactivity (as shown in Fig. 4b). After 90 min TNT layers decorated with 20, 60, 180 and 360 $MoTe_2$ ALD cycles rendered a drop of the MB concentration to approx. 46.4, 20.4, 2.6 and 49.4% of its initial value, respectively. The poor catalytic performance under visible light exhibited by the TNT layers decorated with 360 ALD cycles is ascribed to the shorter lifetime of the photogenerated redox active species produced by the larger $MoTe_2$ nanosheets size, as described in Section 3.2. TNT layers decorated with 20 and 60 $MoTe_2$ ALD cycles displayed a deviation from first-pseudo order kinetics, which was also recently observed in 2D $MoSe_2$ nanosheets grown by ALD on TNT layers [79]. Therein, after ruling out experimentally the (photo)degradation of the $MoTe_2$, the experimental data were found to exhibit a $\sqrt{t}$ time dependence following the next expression:

$$\ln(C/Co) = -A\sqrt{t} \quad (3)$$

where ln (C/C_o) is the MB degradation rate as in Eq. (2) and A is a coefficient, whose value allows best curve fitting. The coefficient A^2 (with the same units as a reaction rate coefficient of first order, i.e. min^{-1}) was related to the degradation rate and the number of available catalytic active sites. Basically, Eq. (3) describes a diffusion-controlled catalytic process to which the experimental data from ALD $MoTe_2$/TNT layers decorated with 20 and 60 cycles fitted well, and whose corresponding A^2 coefficient values are shown in the Table 2.

The physical and chemical stability of $MoTe_2$/TNT layers was assessed by SEM and XPS analysis conducted before and after photocatalytic performance. XPS revealed a significant oxidation degree of the $MoTe_2$ after photocatalytic performance, indicating a poor chemical stability of the $MoTe_2$ in aqueous solution (see Fig. S17). The lack of published works in the literature reporting the photocatalytic properties of $MoTe_2$ towards MB degradation prevent any performance comparison.

3.5. Electrocatalytic properties

The electrocatalytic activity of the $MoTe_2$/ TNT layers was assessed by HER process, whose steps in acidic solution can be summarized by the Eqs. (4)–(6) shown below. Thus, adsorbed hydrogen is formed in a first step via the reduction of hydronium ion (H_3O^+) on a catalyst active site (the discharge step or Volmer reaction, Eq. (4)), followed by molecular H_2 formation, which might occur either via electrochemical desorption by the transfer of a second hydronium ion (Heyrovsky step, Eq. (5)) or by the recombination of two adsorbed protons (Tafel step, Eq. (6)):

$$H_3O^+ + e^- + * \rightarrow H_{ads} + H_2O \quad (4)$$

$$H_{ads} + H_3O^+ + e^- \rightarrow H_2 + H_2O \quad (5)$$

$$2H_{ads} \rightarrow H_2 \quad (6)$$

where * denotes an active site on the catalyst surface and H_{ads} an adsorbed hydrogen atom on a catalyst active site. The HER polarization curves within a cathodic potential window and the corresponding Tafel slopes obtained in 0.5 M H_2SO_4 solution for the different $MoTe_2$/TNT layers samples are shown in Fig. 5a and b, respectively. The strong reduction of the overpotential values required to deliver a current density of −10 mA cm^{-2} as compared to that one of the blank TNT layers, verified the benefits on the electrocatalytic properties of the $MoTe_2$. The corresponding overpotential value and Tafel slope are displayed in Table 3.

The results showed that the lowest overpotential value was obtained for samples with 250 and 500 $MoTe_2$ ALD cycles, while a lower or higher number of $MoTe_2$ ALD cycles led to an increase of the overpotential value. The underlying reason for the lower performance of $MoTe_2$ ALD cycles (60) is the smaller size of $MoTe_2$ nanosheets. Those offer a lower number of catalytic active sites for H adsorption and the HER slowed down, as Tafel slope value indicated. In contrast, a higher number of $MoTe_2$ ALD cycles (1000 and 1500) exhibited an increased overpotential value suggesting lower electrical conductivity, a fact accounted to larger $MoTe_2$ nanosheets comprised of a higher number of stacked layers. Nevertheless, the HER kinetics exhibited by most samples was comparable (similar Tafel slope values), including the samples with a high number of $MoTe_2$ ALD cycles (1000 and 1500). Those own larger $MoTe_2$ nanosheets that provide a higher number of available catalytic active sites for H adsorption. The experimental Tafel slope values (~ 110–100 mV/dec) indicated that Volmer reaction (Eq. (4)) was the rate-determining step, i.e., the charge transfer reaction. $MoTe_2$/TNT layers HER electrochemical properties were compared to $MoTe_2$ HER results reported in the literature (see Table 4). However, such comparison is difficult, basically due to several factors such as $MoTe_2$ synthesis method, morphology, and supporting material, among others.

The assessment of the long-term stability in 0.5 M H_2SO_4 was carried out applying a constant cathodic overpotential value of −550 mV for 48 h to the $MoTe_2$/TNT layers with 1500 ALD cycles. Remarkably, a constant and gradual enhancement of the HER electrochemical activity over time was observed and illustrated by a dramatic increasing of the initial current density of ~ 840% (from 2.8 to 23.5 mA cm^{-2}) as shown in Fig. 5c. In the case of the $MoTe_2$/TNT layers with 250 ALD cycles the current density enhancement after 48 h was ~325% (see Fig. S18a). Cyclic voltammetry measurements using the $MoTe_2$/TNT layers with 1500 ALD cycles, conducted before and after chronoamperometry, corroborated the electrochemical activation by an overpotential value of −212 mV, what means a reduction of ~45% of the initial value (−479 mV before electrochemical activation) as displayed in Fig. 5d. One must note that the corresponding Tafel slope after chronoamperometry (see Fig. S19) did not vary (~ 102 mV/dec), disclosing that electrochemical activation did not affect the rate-determining step (Volmer step). Interestingly, the potential sweep (in the potential range from +0.1 to −1 V) applied by cyclic voltammetry also triggered an electrochemical activation as shown

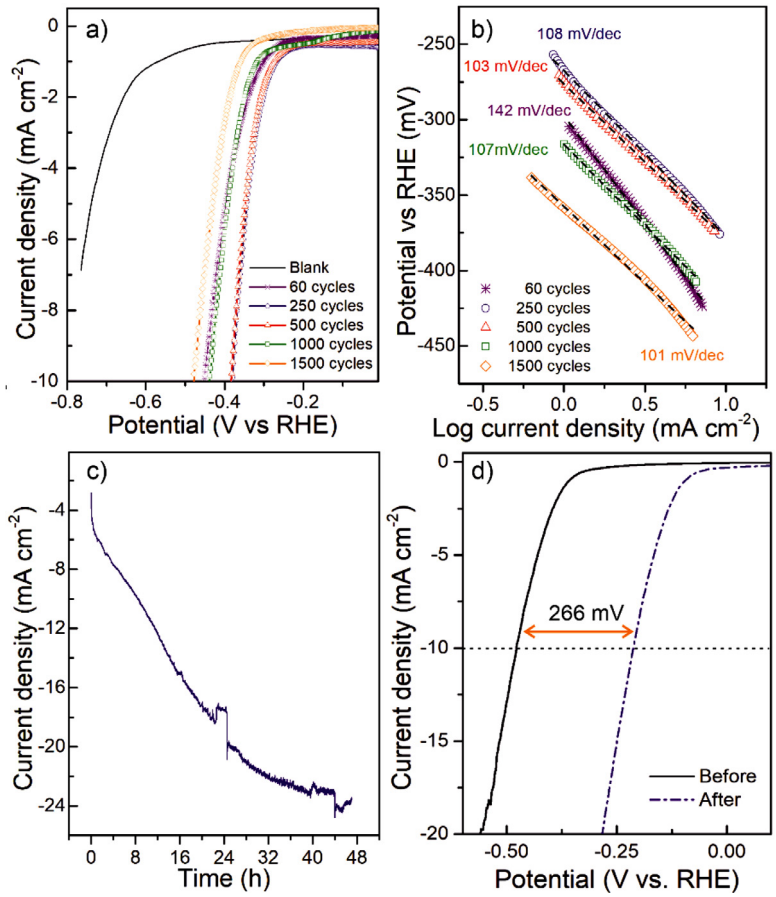

Fig. 5. (a) HER polarization curves obtained for TNT layers decorated with different number of $MoTe_2$ ALD cycles and (b) the corresponding Tafel plots in 0.5 M H_2SO_4 solution; dashed lines are provided as a guide to the eye. (c) Chronoamperometry profile over 48 h applying an overpotential value of −550 mV using $MoTe_2$/TNT layers with 1500 ALD cycles exhibiting the gradual and constant electrochemical activation undergone by the sample. (d) Comparison of the current densities achieved by $MoTe_2$/TNT layers with 1500 ALD cycles before and after the chronoamperometric performance revealing a drop of 266 mV in the initial overpotential at −10 mA cm^{-2} value.

Table 4
Comparison of characteristic electrochemical parameters of $MoTe_2$/TNT layers with reports in the literature on the use of $MoTe_2$ as catalysts for HER.

Catalyst	$MoTe_2$ synthesis method	Overpotential at −10 mA cm^{-2} (mV vs RHE)	Tafel slope (mV/dec)	Reference
1T' - $MoTe_2$/C cloth	CVD	−230.7	127.1	[39]
2H - $MoTe_2$	Flux method	−650	184	[40]
1T' - $MoTe_2$	Flux method	−356	127	[40]
1T' - $MoTe_2$	Electrochemical method	−356	127	[41]
Pt/1T' - $MoTe_2$	Electrochemical method	−23	22	[41]
$MoTe_2$/graphene	Microwave-synthesis	−150	94.5	[44]
1T′- $MoTe_2$/glassy C	Chemical exfoliation	−380	57	[45]
$MoTe_2$	Liquid exfoliation	−309	118.9	[46]
1T' - $MoTe_2$/PyC/SiO_2	Electrodeposition& thermal treatment	−460 (vs Ag/AgCl)	69	[47]
2H - $MoTe_2$	Thermal treatment powder mixture	−650	159	[51]
1T' - $MoTe_2$	Thermal treatment powder mixture	−340	78	[51]
$MoTe_2$/TiO_2 NTs	ALD	−373	108	This work

in the Fig. S18b. Therein, a reduction of ~80 mV of the overpotential value (i.e., a drop of ~ 20% of the initial value) at a current density of −10 mA cm^{-2} was found after running cyclic voltammetry (300 CVs) with the $MoTe_2$/TNT layers decorated with 250 $MoTe_2$ ALD cycles (see inlet Fig. S18b).

In order to evaluate the chemical and structural stability of $MoTe_2$/TNT layers with 1500 ALD cycles sample after chronoamperometry performance, XPS and SEM analyses were conducted and shown in Fig. S20. SEM images exhibited excellent physical integrity of both the TNT layers and the ALD $MoTe_2$ nanosheets. Furthermore, XPS high-resolution spectrum of Mo 3d showed an excellent chemical stability with no changes in the chemical surface composition. Notably, XPS high-resolution spectrum of Te 3d revealed a meaningful strong decrease of the Te-O peaks, i.e., Te sites underwent a reduction process. Hence, the XPS experimental results suggested that the origin of the electrochemical activation would stem from electron doping of Te sites under reductive bias triggering the electrochemical activity of the ALD $MoTe_2$ nanosheets. This phenomenon is in line with recently reported works on nanocrystalline $MoTe_2$ by Mc Glynn et al., who ascribed the origin of $MoTe_2$ electrochemical activation to be of electronic nature rather than chemical or morphological changes of the catalyst [42,43]. Therein, computational analysis suggested that the origin of the electrochemical activation under the application of reductive bias was an electron doping, along with a $MoTe_2$ distortion caused by H adsorption on certain Te sites. Most remarkable,

it was claimed that the electrochemical improvement occurred on the inactive basal planes rather than on edge sites. This scenario would match well with the physical interpretation by which the aforementioned overpotential drop and gradual and constant increase of the current, would be caused by the constant formation of available new active sites to the H adsorption.

4. Conclusions

The synthesis of $MoTe_2$ by means of ALD was demonstrated for the first time. The growth of $MoTe_2$ as 2D flaky nanosheets out-of-plane oriented was obtained by combining commercial Mo precursor with newly synthesized Te precursor. The nanosheet morphology enhanced the number of active edges sites, and out-of-plane orientation maximized the exposed active edges what boosted the $MoTe_2$ nanosheets catalytic properties. The $MoTe_2$ photo- and electrocatalytic properties were assessed by $MoTe_2$/TNT layers heterostructures fabricated by a fast and simple process. Excellent photo- and electrocatalytic properties were revealed towards organic dye degradation and hydrogen evolution reaction. Remarkably, electrochemical activation was observed applying both constant cathodic potential and cyclic voltammetry. Subsequent XPS analysis demonstrated an excellent chemical stability of the ALD $MoTe_2$ nanosheets and suggested a Te reduction effect observed under cathodic bias as a potential origin of the electrochemical activity.

Declaration of Competing Interest

The authors declare that they have no known competing financial interests or personal relationships that could have appeared to influence the work reported in this paper.

CRediT authorship contribution statement

Raul Zazpe: Conceptualization, Writing – original draft, Investigation, Visualization. **Hanna Sopha:** Investigation, Validation, Writing – review & editing. **Jaroslav Charvot:** Investigation, Methodology. **Richard Krumpolec:** Investigation, Methodology. **Jhonatan Rodriguez-Pereira:** Investigation. **Jan Michalička:** Investigation. **Jan Mistrík:** Investigation. **Dominik Bača:** Investigation. **Martin Motola:** Investigation. **Filip Bureš:** Conceptualization, Methodology, Resources, Writing – review & editing, Supervision. **Jan M. Macak:** Conceptualization, Writing – review & editing, Resources, Supervision.

Acknowledgements

The authors acknowledge the financial support from the Czech Science Foundation (1803881S) and the Ministry of Education, Youth and Sports of the Czech Republic (MEYS CR, projects LM2018097, LM2018103, CZ.02.1.01/0.0/0.0/17_048/0007421). CzechNanoLab project LM2018110 funded by MEYS CR is gratefully acknowledged for the financial support of the measurements/sample fabrication at CEITEC Nano Research Infrastructure. We thank Mr. L. Hromadko for SEM and XRD measurements and Dr. David Pavlinak for Raman analyses (results not shown here) and Dr. M. Klikar for DSC measurements.

Supplementary materials

Supplementary material associated with this article can be found, in the online version, at doi:10.1016/j.apmt.2021.101017.

References

[1] W. Choi, N. Choudhary, G.H. Han, J. Park, D. Akinwande, Y.H. Lee, Recent development of two-dimensional transition metal dichalcogenides and their applications, Mater. Today. 20 (2017) 116–130 https://doi.org/, doi:10.1016/j.mattod.2016.10.002.
[2] S. Manzeli, D. Ovchinnikov, D. Pasquier, O.V. Yazyev, A. Kis, 2D transition metal dichalcogenides, Nat. Rev. Mater. 2 (2017) 17033 https://doi.org/, doi:10.1038/natrevmats.2017.33.
[3] Q.H. Wang, K. Kalantar-Zadeh, A. Kis, J.N. Coleman, M.S. Strano, Electronics and optoelectronics of two-dimensional transition metal dichalcogenides, Nat. Nanotechnol. 7 (2012) 699–712 https://doi.org/, doi:10.1038/nnano.2012.193.
[4] K.F. Mak, J. Shan, Photonics and optoelectronics of 2D semiconductor transition metal dichalcogenides, Nat. Photonics. 10 (2016) 216–226 https://doi.org/, doi:10.1038/nphoton.2015.282.
[5] J. Ping, Z. Fan, M. Sindoro, Y. Ying, H. Zhang, Recent advances in sensing applications of two-dimensional transition metal dichalcogenide nanosheets and their composites, Adv. Funct. Mater. 27 (2017) 1605817 https://doi.org/, doi:10.1002/adfm.201605817.
[6] M. Pumera, Z. Sofer, A. Ambrosi, Layered transition metal dichalcogenides for electrochemical energy generation and storage, J. Mater. Chem. A. 2 (2014) 8981–8987 https://doi.org/, doi:10.1039/C4TA00652F.
[7] Q. Lu, Y. Yu, Q. Ma, B. Chen, H. Zhang, 2D transition-metal-dichalcogenide-nanosheet-based composites for photocatalytic and electrocatalytic hydrogen evolution reactions, Adv. Mater. 28 (2016) 1917–1933 https://doi.org/, doi:10.1002/adma.201503270.
[8] B. Luo, G. Liu, L. Wang, Recent advances in 2D materials for photocatalysis, Nanoscale. 8 (2016) 6904–6920. https://doi.org/ 10.1039/C6NR00546B.
[9] G.W. Shim, W. Hong, S.Y. Yang, S.-Y.Y. Choi, Tuning the catalytic functionality of transition metal dichalcogenides grown by chemical vapour deposition, J. Mater. Chem. A. 5 (2017) 14950–14968 https://doi.org/, doi:10.1039/C7TA03039H.
[10] S.H. Noh, J. Hwang, J. Kang, M.H. Seo, D. Choi, B. Han, Tuning the catalytic activity of heterogeneous two-dimensional transition metal dichalcogenides for hydrogen evolution, J. Mater. Chem. A. 6 (2018) 20005–20014 https://doi.org/, doi:10.1039/C8TA07141A.
[11] X. Zou, Y. Zhang, Noble metal-free hydrogen evolution catalysts for water splitting, Chem. Soc. Rev. 44 (2015) 5148–5180 https://doi.org/, doi:10.1039/C4CS00448E.
[12] Y. Yan, B.Y. Xia, B. Zhao, X. Wang, A review on noble-metal-free bifunctional heterogeneous catalysts for overall electrochemical water splitting, J. Mater. Chem. A. 4 (2016) 17587–17603 https://doi.org/, doi:10.1039/C6TA08075H.
[13] S.X. Leong, C.C. Mayorga-Martinez, X. Chia, J. Luxa, Z. Sofer, M. Pumera, 2H → 1T Phase Change in Direct Synthesis of WS 2 nanosheets via solution-based electrochemical exfoliation and their catalytic properties, ACS Appl. Mater. Interfaces. 9 (2017) 26350–26356 https://doi.org/, doi:10.1021/acsami.7b06898.
[14] B. Mahler, V. Hoepfner, K. Liao, G.A. Ozin, Colloidal Synthesis of 1T-WS 2 and 2H-WS 2 nanosheets: applications for photocatalytic hydrogen evolution, J. Am. Chem. Soc. 136 (2014) 14121–14127 https://doi.org/, doi:10.1021/ja506261t.
[15] J. Mao, Y. Wang, Z. Zheng, D. Deng, The rise of two-dimensional MoS_2 for catalysis, Front. Phys. 13 (2018) 138118 https://doi.org/, doi:10.1007/s11467-018-0812-0.
[16] G. Li, D. Zhang, Q. Qiao, Y. Yu, D. Peterson, A. Zafar, R. Kumar, S. Curtarolo, F. Hunte, S. Shannon, Y. Zhu, W. Yang, L. Cao, All the catalytic active sites of MoS_2 for hydrogen evolution, J. Am. Chem. Soc. 138 (2016) 16632–16638 https://doi.org/, doi:10.1021/jacs.6b05940.
[17] A. Eftekhari, Molybdenum diselenide (MoSe2) for energy storage, catalysis, and optoelectronics, Appl. Mater. Today. 8 (2017) 1–17 https://doi.org/, doi:10.1016/j.apmt.2017.01.006.
[18] J.-.H. Huang, H.-.H. Hsu, D. Wang, W.-.T. Lin, C.-.C. Cheng, Y.-J. Lee, T.-.H. Hou, Polymorphism control of layered $MoTe_2$ through two-dimensional solid-phase crystallization, Sci. Rep. 9 (2019) 8810 https://doi.org/, doi:10.1038/s41598-019-45142-x.
[19] K.-A.N. Duerloo, Y. Li, E.J. Reed, Structural phase transitions in two-dimensional Mo- and W-dichalcogenide monolayers, Nat. Commun. 5 (2014) 4214 https://doi.org/, doi:10.1038/ncomms5214.
[20] C. Ruppert, O.B. Aslan, T.F. Heinz, Optical properties and band gap of single- and few-layer MoTe2 crystals, Nano Lett. 14 (2014) 6231–6236. https://doi.org/10.1021/nl502557g.
[21] J. Gusakova, X. Wang, L.L. Shiau, A. Krivosheeva, V. Shaposhnikov, V. Borisenko, V. Gusakov, B.K. Tay, Electronic properties of bulk and monolayer tmds: theoretical study within DFT framework (GVJ-2e Method), Phys. Status Solidi. 214 (2017) 1700218 https://doi.org/, doi:10.1002/pssa.201700218.
[22] D.H. Keum, S. Cho, J.H. Kim, D.-.H. Choe, H.-.J. Sung, M. Kan, H. Kang, J.-.Y. Hwang, S.W. Kim, H. Yang, K.J. Chang, Y.H. Lee, Bandgap opening in few-layered monoclinic MoTe2, Nat. Phys. 11 (2015) 482–486. https://doi.org/10.1038/nphys3314.
[23] T.J.S. Anand, N.H. Mazlan, Electro Synthesized $MoTe_2$ Thin Films and their Semiconductor Studies towards Photoelectrochemical Cell, Adv. Mater. Res. 845 (2013) 392–397 https://doi.org/, doi:10.4028/www.scientific.net/AMR.845.392.
[24] S. Hussain, S.A. Patil, D. Vikraman, N. Mengal, H. Liu, W. Song, K.-.S. An, S.H. Jeong, H.-.S. Kim, J. Jung, Large area growth of $MoTe_2$ films as high performance counter electrodes for dye-sensitized solar cells, Sci. Rep. 8 (2018) 29 https://doi.org/, doi:10.1038/s41598-017-18067-6.

[25] J.Y. Lim, A. Pezeshki, S. Oh, J.S. Kim, Y.T. Lee, S. Yu, D.K. Hwang, G.-.H. Lee, H.J. Choi, S. Im, Homogeneous 2D MoTe2 P-N Junctions and CMOS Inverters formed by atomic-layer-deposition-induced doping, Adv. Mater. 29 (2017) 1701798. https://doi.org/ 10.1002/adma.201701798.

[26] Y.-.F. Lin, Y. Xu, C.-.Y. Lin, Y.-.W. Suen, M. Yamamoto, S. Nakaharai, K. Ueno, K. Tsukagoshi, Origin of noise in layered $MoTe_2$ transistors and its possible use for environmental sensors, Adv. Mater. 27 (2015) 6612–6619 https://doi.org/, doi:10.1002/adma.201502677.

[27] I. Shackery, A. Pezeshki, J.Y. Park, U. Palanivel, H.J. Kwon, H.S. Yoon, S. Im, J.S. Cho, S.C. Jun, Few-layered α-MoTe 2 Schottky junction for a high sensitivity chemical-vapour sensor, J. Mater. Chem. C. 6 (2018) 10714–10722 https://doi.org/, doi:10.1039/C8TC02635A.

[28] Y.-.Q. Bie, G. Grosso, M. Heuck, M.M. Furchi, Y. Cao, J. Zheng, D. Bunandar, E. Navarro-Moratalla, L. Zhou, D.K. Efetov, T. Taniguchi, K. Watanabe, J. Kong, D. Englund, P. Jarillo-Herrero, A MoTe2-based light-emitting diode and photodetector for silicon photonic integrated circuits, Nat. Nanotechnol. 12 (2017) 1124–1129 https://doi.org/, doi:10.1038/nnano.2017.209.

[29] E. Wu, Y. Xie, B. Yuan, H. Zhang, X. Hu, J. Liu, D. Zhang, Ultrasensitive and fully reversible NO_2 gas sensing based on p-type $MoTe_2$ under ultraviolet illumination, ACS Sensors 3 (2018) 1719–1726 https://doi.org/, doi:10.1021/acssensors.8b00461.

[30] S. Fathipour, N. Ma, W.S. Hwang, V. Protasenko, S. Vishwanath, H.G. Xing, H. Xu, D. Jena, J. Appenzeller, A. Seabaugh, Exfoliated multilayer $MoTe_2$ field-effect transistors, Appl. Phys. Lett. 105 (2014) 192101 https://doi.org/, doi:10.1063/1.4901527.

[31] T.J. Octon, V.K. Nagareddy, S. Russo, M.F. Craciun, C.D. Wright, Fast high-responsivity few-layer $MoTe_2$ photodetectors, Adv. Opt. Mater. 4 (2016) 1750–1754 https://doi.org/, doi:10.1002/adom.201600290.

[32] N.R. Pradhan, D. Rhodes, S. Feng, Y. Xin, S. Memaran, B.-.H. Moon, H. Terrones, M. Terrones, L. Balicas, Field-effect transistors based on few-layered α-MoTe2, ACS Nano. 8 (2014) 5911–5920. https://doi.org/ 10.1021/nn501013c.

[33] J. Xu, J. Zhang, W. Zhang, C.-.S. Lee, Interlayer nanoarchitectonics of two-dimensional transition-metal dichalcogenides nanosheets for energy storage and conversion applications, Adv. Energy Mater. 7 (2017) 1700571 https://doi.org/, doi:10.1002/aenm.201700571.

[34] E.-.K. Kim, S.J. Yoon, H.T. Bui, S.A. Patil, C. Bathula, N.K. Shrestha, H. Im, S.-.H. Han, Epitaxial electrodeposition of single crystal MoTe2 nanorods and Li+ storage feasibility, J. Electroanal. Chem. 878 (2020) 114672 https://doi.org/, doi:10.1016/j.jelechem.2020.114672.

[35] N. Ma, X.-.Y. Jiang, L. Zhang, X.-.S. Wang, Y.-.L. Cao, X.-.Z. Zhang, Novel 2D layered molybdenum ditelluride encapsulated in few-layer graphene as high-performance anode for lithium-ion batteries, Small 14 (2018) 1703680 https://doi.org/, doi:10.1002/smll.201703680.

[36] M.R. Panda, R. Gangwar, D. Muthuraj, S. Sau, D. Pandey, A. Banerjee, A. Chakrabarti, A. Sagdeo, M. Weyland, M. Majumder, Q. Bao, S. Mitra, High performance lithium-ion batteries using layered 2H-$MoTe_2$ as anode, Small 16 (2020) 1–16 https://doi.org/, doi:10.1002/smll.202002669.

[37] M. Liu, Z. Wang, J. Liu, G. Wei, J. Du, Y. Li, C. An, J. Zhang, Synthesis of few-layer 1T′-$MoTe_2$ ultrathin nanosheets for high-performance pseudocapacitors, J. Mater. Chem. A. 5 (2017) 1035–1042 https://doi.org/, doi:10.1039/C6TA08206H.

[38] S.S. Karade, B.R. Sankapal, Materials mutualism through EDLC-Behaved MWCNTs with Pseudocapacitive $MoTe_2$ nanopebbles: enhanced supercapacitive performance, ACS Sustain. Chem. Eng. 6 (2018) 15072–15082 https://doi.org/, doi:10.1021/acssuschemeng.8b03366.

[39] D. Lu, X. Ren, L. Ren, W. Xue, S. Liu, Y. Liu, Q. Chen, X. Qi, J. Zhong, Direct vapor deposition growth of 1T′ $MoTe_2$ on carbon cloth for electrocatalytic hydrogen evolution, ACS Appl. Energy Mater. 3 (2020) 3212–3219 https://doi.org/, doi:10.1021/acsaem.9b01589.

[40] J. Seok, J.-.H. Lee, S. Cho, B. Ji, H.W. Kim, M. Kwon, D. Kim, Y.-.M. Kim, S.H. Oh, S.W. Kim, Y.H. Lee, Y.-.W. Son, H. Yang, Active hydrogen evolution through lattice distortion in metallic $MoTe_2$, 2D Mater., 4, 2017 https://doi.org/, doi:10.1088/2053-1583/aa659d.

[41] J. Seok, J.-.H. Lee, D. Bae, B. Ji, Y.-.W. Son, Y.H. Lee, H. Yang, S. Cho, Hybrid catalyst with monoclinic $MoTe_2$ and platinum for efficient hydrogen evolution, APL Mater 7 (2019) 071118 https://doi.org/, doi:10.1063/1.5094957.

[42] J.C. McGlynn, M. Friskey, A.Y. Ganin, Parameter optimisation for electrochemically activated MoTe2, Sustain. Energy Fuels. 4 (2020) 4473–4477. https://doi.org/ 10.1039/D0SE00684J.

[43] J.C. McGlynn, T. Dankwort, L. Kienle, N.A.G. Bandeira, J.P. Fraser, E.K. Gibson, I. Cascallana-Matías, K. Kamarás, M.D. Symes, H.N. Miras, A.Y. Ganin, The rapid electrochemical activation of $MoTe_2$ for the hydrogen evolution reaction, Nat. Commun. 10 (2019) 4916 https://doi.org/, doi:10.1038/s41467-019-12831-0.

[44] S. Sarwar, A. Ali, Z. Liu, J. Li, S. Uprety, H. Lee, R. Wang, M. Park, M.J. Bozack, A.J. Adamczyk, X. Zhang, Towards thermoneutral hydrogen evolution reaction using noble metal free molybdenum ditelluride/graphene nanocomposites, J. Colloid Interface Sci. 581 (2021) 847–859 https://doi.org/, doi:10.1016/j.jcis.2020.07.122.

[45] J. Luxa, P. Vosecký, V. Mazánek, D. Sedmidubský, M. Pumera, P. Lazar, Z. Sofer, Layered transition-metal ditellurides in electrocatalytic applications—contrasting properties, ACS Catal. 7 (2017) 5706–5716. https://doi.org/10.1021/acscatal.7b02080.

[46] H. Qiao, Z. Huang, S. Liu, Y. Liu, J. Li, X. Qi, Liquid-exfoliated molybdenum telluride nanosheets with superior electrocatalytic hydrogen evolution performances, Ceram. Int. 44 (2018) 21205–21209 https://doi.org/, doi:10.1016/j.ceramint.2018.08.166.

[47] J.B. Mc Manus, G. Cunningham, N. McEvoy, C.P. Cullen, F. Gity, M. Schmidt, D. McAteer, D. Mullarkey, I.V. Shvets, P.K. Hurley, T. Hallam, G.S. Duesberg, Growth of 1T′ MoTe 2 by thermally assisted conversion of electrodeposited tellurium films, ACS Appl. Energy Mater. 2 (2019) 521–530 https://doi.org/, doi:10.1021/acsaem.8b01540.

[48] P. Zhuang, Y. Sun, P. Dong, W. Smith, Z. Sun, Y. Ge, Y. Pei, Z. Cao, P.M. Ajayan, J. Shen, M. Ye, Revisiting the role of active sites for hydrogen evolution reaction through precise defect adjusting, Adv. Funct. Mater. 29 (2019) 1901290 https://doi.org/, doi:10.1002/adfm.201901290.

[49] D. Deng, K.S. Novoselov, Q. Fu, N. Zheng, Z. Tian, X. Bao, Catalysis with two-dimensional materials and their heterostructures, Nat. Nanotechnol. 11 (2016) 218–230 https://doi.org/, doi:10.1038/nnano.2015.340.

[50] S. Aftab, Rabia Samiya, S. Yousuf, M.U. Khan, R. Khawar, A. Younus, M. Manzoor, M.W. Iqbal, M.Z. Iqbal, Carrier polarity modulation of molybdenum ditelluride (MoTe 2) for phototransistor and switching photodiode applications, Nanoscale 12 (2020) 15687–15696 https://doi.org/, doi:10.1039/D0NR03904G.

[51] J.C. McGlynn, I. Cascallana-Matías, J.P. Fraser, I. Roger, J. McAllister, H.N. Miras, M.D. Symes, A.Y. Ganin, Molybdenum ditelluride rendered into an efficient and stable electrocatalyst for the hydrogen evolution reaction by polymorphic control, Energy Technol 6 (2018) 345–350 https://doi.org/, doi:10.1002/ente.201700489.

[52] J.C. Park, S.J. Yun, H. Kim, J.-.H. Park, S.H. Chae, S.-.J. An, J.-.G. Kim, S.M. Kim, K.K. Kim, Y.H. Lee, Phase-engineered synthesis of centimeter-scale 1T′- and 2H-molybdenum ditelluride thin films, ACS Nano. 9 (2015) 6548–6554. https://doi.org/ 10.1021/acsnano.5b02511.

[53] L. Zhou, K. Xu, A. Zubair, A.D. Liao, W. Fang, F. Ouyang, Y.-.H. Lee, K. Ueno, R. Saito, T. Palacios, J. Kong, M.S. Dresselhaus, Large-area synthesis of high-quality uniform few-layer $MoTe_2$, J. Am. Chem. Soc. 137 (2015) 11892–11895 https://doi.org/, doi:10.1021/jacs.5b07452.

[54] A. Roy, H.C.P. Movva, B. Satpati, K. Kim, R. Dey, A. Rai, T. Pramanik, S. Guchhait, E. Tutuc, S.K. Banerjee, Structural and electrical properties of $MoTe_2$ and $MoSe_2$ grown by molecular beam epitaxy, ACS Appl. Mater. Interfaces 8 (2016) 7396–7402 https://doi.org/, doi:10.1021/acsami.6b00961.

[55] C. Detavernier, J. Dendooven, S.P. Sree, K.F. Ludwig, J.A. Martens, Tailoring nanoporous materials by atomic layer deposition, Chem. Soc. Rev. 40 (2011) 5242–5253 https://doi.org/, doi:10.1039/c1cs15091j.

[56] F. Dvorak, R. Zazpe, M. Krbal, H. Sopha, J. Prikryl, S. Ng, L. Hromadko, F. Bures, J.M. Macak, One-dimensional anodic TiO_2 nanotubes coated by atomic layer deposition: towards advanced applications, Appl. Mater. Today. 14 (2019) 1–20 https://doi.org/, doi:10.1016/j.apmt.2018.11.005.

[57] V. Cremers, R.L. Puurunen, J. Dendooven, Conformality in atomic layer deposition: current status overview of analysis and modelling, Appl. Phys. Rev. 6 (2019) 021302 https://doi.org/, doi:10.1063/1.5060967.

[58] J. Cai, X. Han, X. Wang, X. Meng, Atomic layer deposition of two-dimensional layered materials: processes, growth mechanisms, and characteristics, Matter, 2020 https://doi.org/, doi:10.1016/j.matt.2019.12.026.

[59] G.H. Park, K. Nielsch, A. Thomas, 2D transition metal dichalcogenide thin films obtained by chemical gas phase deposition techniques, Adv. Mater. Interfaces. (2019) https://doi.org/, doi:10.1002/admi.201800688.

[60] M. Mattinen, M. Leskelä, M. Ritala, Atomic layer deposition of 2D metal dichalcogenides for electronics, catalysis, energy storage, and beyond, Adv. Mater. Interfaces (2021) 2001677 https://doi.org/, doi:10.1002/admi.202001677.

[61] S. Das, H. Sopha, M. Krbal, R. Zazpe, V. Podzemna, J. Prikryl, J.M. Macak, Electrochemical infilling of CuInSe2 within TiO2 Nanotube layers and subsequent photoelectrochemical studies, ChemElectroChem. 4 (2017) 495–499. https://doi.org/ 10.1002/celc.201600763.

[62] M. Motola, L. Hromadko, J. Prikryl, H. Sopha, M. Krbal, J.M. Macak, Intrinsic properties of high-aspect ratio single- and double-wall anodic TiO_2 nanotube layers annealed at different temperatures, Electrochim. Acta. 352 (2020) 136479 https://doi.org/, doi:10.1016/j.electacta.2020.136479.

[63] U. Herzog, G. Rheinwald, Five- and six-membered ring Group 14 chalcogenides of the types, J. Organomet. Chem. 627 (2001) 23–36.

[64] M.R. Detty, M.D. Seidler, Bis(trialkylsilyl) chalcogenides. 1. Preparation and reduction of group VIA oxides, J. Org. Chem. 47 (1982) 1354–1356 https://doi.org/, doi:10.1021/jo00346a041.

[65] V. Pore, T. Hatanpää, M. Ritala, M. Leskela, Atomic layer deposition of metal tellurides and selenides using alkylsilyl compounds of tellurium and selenium, J. Am. Chem. Soc. 131 (2009) 3478–3480 https://doi.org/, doi:10.1021/ja8090388.

[66] S. Yoo, C. Yoo, E.S. Park, W. Kim, Y.K. Lee, C.S. Hwang, Chemical interactions in the atomic layer deposition of Ge-Sb-Se-Te films and their ovonic threshold switching behavior, J. Mater. Chem. C. 6 (2018) 5025–5032 https://doi.org/, doi:10.1039/c8tc01041b.

[67] M. Rusek, T. Komossa, G. Bendt, S. Schulz, Bismuth amides as promising ALD precursors for Bi_2Te_3 films, J. Cryst. Growth. 470 (2017) 128–134 https://doi.org/, doi:10.1016/j.jcrysgro.2017.04.019.

[68] C.H. Naylor, W.M. Parkin, J. Ping, Z. Gao, Y.R. Zhou, Y. Kim, F. Streller, R.W. Carpick, A.M. Rappe, M. Drndić, J.M. Kikkawa, A.T.C. Johnson, Monolayer single-crystal 1T′-$MoTe_2$ grown by chemical vapor deposition exhibits weak antilocalization effect, Nano Lett. 16 (2016) 4297–4304 https://doi.org/, doi:10.1021/acs.nanolett.6b01342.

[69] Y. Tan, F. Luo, M. Zhu, X. Xu, Y. Ye, B. Li, G. Wang, W. Luo, X. Zheng, N. Wu, Y. Yu, S. Qin, X.-.A. Zhang, Controllable 2H-to-1T′ phase transition in few-layer MoTe2, Nanoscale. 10 (2018) 19964–19971. https://doi.org/10.1039/C8NR06115G.

[70] G.H. Han, D.H. Keum, J. Zhao, B.G. Shin, S. Song, J.J. Bae, J. Lee, J.H. Kim, H. Kim, B.H. Moon, Y.H. Lee, Absorption dichroism of monolayer 1T′-MoTe 2 in visible range, 2D Mater. 3 (2016) 031010. https://doi.org/ 10.1088/2053-1583/3/3/031010.

[71] K. Chen, Z. Chen, X. Wan, Z. Zheng, F. Xie, W. Chen, X. Gui, H. Chen, W. Xie, J. Xu, A simple method for synthesis of high-quality millimeter-scale 1T′ transition-metal telluride and near-field nanooptical properties, Adv. Mater. 29 (2017) 1700704 https://doi.org/, doi:10.1002/adma.201700704.

[72] J. Charvot, D. Pokorný, R. Zazpe, R. Krumpolec, D. Pavliňák, L. Hromádko, J. Přikryl, J. Rodriguez-Pereira, M. Klikar, V. Jelínková, J.M. Macak, F. Bureš, Cyclic Silylselenides: convenient selenium precursors for atomic layer deposition, Chempluschem 85 (2020) 576–579 https://doi.org/, doi:10.1002/cplu.202000108.

[73] B. Chen, H. Sahin, A. Suslu, L. Ding, M.I. Bertoni, F.M. Peeters, S. Tongay, Environmental Changes in $MoTe_2$ excitonic dynamics by defects-activated molecular interaction, ACS Nano 9 (2015) 5326–5332 https://doi.org/, doi:10.1021/acsnano.5b00985.

[74] S. Ng, P. Kuberský, M. Krbal, J. Prikryl, V. Gärtnerová, D. Moravcová, H. Sopha, R. Zazpe, F.K. Yam, A. Jäger, L. Hromádko, L. Beneš, A. Hamáček, J.M. Macak, ZnO Coated Anodic 1D TiO_2 Nanotube Layers: efficient photoelectrochemical and gas sensing heterojunction, Adv. Eng. Mater. 20 (2018) 1700589 https://doi.org/, doi:10.1002/adem.201700589.

[75] R. Zazpe, H. Sopha, J. Prikryl, M. Krbal, J. Mistrik, F. Dvorak, L. Hromadko, J.M. Macak, A 1D conical nanotubular TiO_2/CdS heterostructure with superior photon-to-electron conversion, Nanoscale 10 (2018) 16601–16612 https://doi.org/, doi:10.1039/c8nr02418a.

[76] M. Krbal, S. Ng, M. Motola, L. Hromadko, F. Dvorak, V. Prokop, H. Sopha, J.M. Macak, Sulfur treated 1D anodic TiO_2 nanotube layers for significant photo- and electroactivity enhancement, Appl. Mater. Today. 17 (2019) 104–111 https://doi.org/, doi:10.1016/j.apmt.2019.07.018.

[77] D.A.G. Bruggeman, Berechnung verschiedener physikalischer Konstanten von heterogenen Substanzen. I. Dielektrizitätskonstanten und Leitfähigkeiten der Mischkörper aus isotropen Substanzen, Ann. Phys. 416 (1935) 636–664 https://doi.org/, doi:10.1002/andp.19354160705.

[78] Y. Li, A. Singh, S. Krylyuk, A. Davydov, R. Jaramillo, Near-infrared photonic phase-change properties of transition metal ditellurides, in: N.P. Kobayashi, A.A. Talin, A.V. Davydov (Eds.), Low-Dimensional Mater. Devices, SPIE, 2019, p. 28, doi:10.1117/12.2532602. https://doi.org/.

[79] R. Zazpe, R. Krumpolec, H. Sopha, J. Rodriguez-Pereira, J. Charvot, L. Hromádko, E. Kolíbalová, J. Michalička, D. Pavliňák, M. Motola, J. Přikryl, M. Krbal, F. Bureš, J.M. Macak, Atomic layer deposition of $MoSe_2$ Nanosheets on TiO_2 nanotube arrays for photocatalytic dye degradation and electrocatalytic hydrogen evolution, ACS Appl. Nano Mater. (2020) acsanm.0c02553https://doi.org/, doi:10.1021/acsanm.0c02553.